npj | computational materials

Article

Published in partnership with the Shanghai Institute of Ceramics of the Chinese Academy of Sciences

https://doi.org/10.1038/s41524-024-01320-8

Automated workflow for analyzing thermodynamic stability in polymorphic perovskite alloys

Luis Octavio de Araujo [1] ✉, Celso R. C. Rêgo [2] ✉, Wolfgang Wenzel [2] ✉, Maurício Jeomar Piotrowski [3] ✉, Alexandre Cavalheiro Dias [4] ✉ & Diego Guedes-Sobrinho [1] ✉

In this first-principles investigation, we explore the polymorphic features of pseudo-cubic alloys, focusing on the impact of mixing organic and inorganic cations on their structural and electronic properties, configurational disorder, and thermodynamic stability. Employing an automated cluster expansion within the generalized quasichemical approximation (GQCA), our results reveal how the effective radius of the organic cation (r_{MA} = 2.15 Å, r_{FA} = 2.53 Å) and its dipole moment (μ_{MA} = 2.15 D, μ_{FA} = 0.25 D), influences Glazer's rotations in the $A_{1-x}Cs_xPbI_3$ (A = MA, FA) sublattice, with MA-based alloy presenting a higher critical temperature (527 K) and being stable for $x > 0.60$ above 200 K, while its FA analog has a lower critical temperature (427.7 K) and is stable for $x < 0.15$ above 100 K. Additionally, polymorphic motifs magnify relativistic effects, impacting the thermodynamic behavior of the systems. Our methodology leverages the SimStack framework, an automated scientific workflow that enables the nuanced modeling of polymorphic alloys. This structured approach allows for comprehensive calculations of thermodynamic properties, phase diagrams, optoelectronic insights, and power conversion efficiencies while meticulously incorporating crucial relativistic effects like spin-orbit coupling (SOC) and quasi-particle corrections. Our findings advocate for the rational design of thermodynamically stable compositions in solar cell applications by calculating power conversion efficiencies using a spectroscopic limited maximum efficiency model, from which we obtained high efficiencies of about 28% (31–32%) for $MA_{1-x}Cs_xPbI_3$ with $0.50 < x < 1.00$ ($FA_{1-x}Cs_xPbI_3$ with $0.0 < x < 0.20$) as thermodynamically stable compositions at room temperature. The workflow's significance is highlighted by a Colab-based notebook, which facilitates the analysis of raw data output, allowing users to delve into the physics of these complex systems. Our work underscores the pivotal role of composition and polymorphic degrees in determining the stability and optoelectronic properties of MHP alloys. It demonstrates the effectiveness of the SimStack workflow in advancing our understanding of these materials.

Metal halide perovskites (MHPs) have emerged as a vital part of photovoltaic devices thanks to their power conversion efficiencies (PCE) exceeding 26%, e.g., for $FAPbI_3$[1]. However, the intrinsic chemical instability of MHPs in correlation with the operation long-time is a challenge for the accomplishment of durable devices[2–4], which is the motivation to implement alloying strategies involving Cs cations with organic candidates to form $A_{1-x}Cs_xPbI_3$ (e.g., A = MA, FA)[5–10]. Withal, the causality correlation between the polymorphic nature of MHPs *in operando* and their electronic properties (connected with the conversion performance) through empirical approaches is not trivial[11–14], which is potentially hampered in the alloying context. Therefore, there is a wide field to develop ab initio protocols to capture this associated polymorphism through a proper construction of the

[1]Department of Chemistry, Federal University of Paraná, Curitiba 81531-980 Paraná, Brazil. [2]Institute of Nanotechnology Hermann-von-Helmholtz-Platz, Karlsruhe Institute of Technology, Karlsruhe, Baden-Württemberg, Germany. [3]Department of Physics, Federal University of Pelotas, Pelotas 96010-900 Rio Grande do Sul, Brazil. [4]Institute of Physics and International Center of Physics, University of Brasília, Brasília 70919-970 DF, Brazil. ✉e-mail: luisaraujo@ufpr.br; celso.rego@kit.edu; wolfgang.wenzel@kit.edu; mauriciomjp@gmail.com; alexandre.dias@unb.br; guedessobrinho@ufpr.br

thermodynamic ensemble of MHP alloys[15–17], at the same time, automation procedures are highly desirable to accelerate data acquisition (especially in industry) from those systems.

The non-dynamic polymorphism concept establishes that cubic MHPs have a local structure different from the global $Pm\bar{3}m$ space group. Recent investigations have proposed the contribution of low symmetry structural motifs through B-metal off-center displacements within octahedra[11], octahedral rotations[18], positional rearrangements of the A cations within the cuboctahedral voids[19], and second-order Jahn-Teller distortions[20], which are not experimentally distinguished by X-ray diffraction (XRD) measurements due to the long coherence length[12]. On the other hand, the impact of those motifs on the thermodynamic stability and electronic properties of MHPs alloys based on an atomistic perspective is scarce, as well as the reliable mapping of the composition dependence through experiments to investigate phase transitions or bowing-like curve (b parameter) for the gap energy requires a high financial cost involving reagents and material characterization[21–25].

Experimentally, $A_{1-x}Cs_xPbI_3$ mixed MHPs were revealed as candidates for solar cells application, with $FA_{1-x}Cs_xPbI_3$ showing no phase segregation for $x < 0.15$ with bandgaps varying only from 1.52 eV to 1.53 eV for these compositions[10,26]. In addition, higher stabilities were found for a perovskite solar cell (PSCs) based on $MA_{0.70}Cs_{0.30}PbI_3$, which retained about 60% of their initial PCE after 500 h at room temperature and humidity of 35–45%, while $MAPbI_3$-based one retained only 30% at the same conditions[27]. XRD studies suggest that Cs incorporation is also beneficial to avoid the decrease in crystallinity in MHPs after 40 days, also leading to the most stable materials against chemical decomposition, improving the material's long-term stability[9]. Synthesis routes for both materials are also experimentally viable, with $(1-x)FAI + xCsI + PbI_2 \longrightarrow FA_{1-x}Cs_xPbI_3$ being employed for $FA_{1-x}Cs_xPbI_3$[10,26,28], while $(1-x)MAI + xCsI + PbI_2 \longrightarrow MA_{1-x}Cs_xPbI_3$ in the presence of butyrolactone is generally used for $MA_{1-x}Cs_xPbI_3$[8,29]. Thus, investing in the study of these systems is promising, contributing significantly to PSCs reaching their long-awaited commercial maturity.

The impact of configurational semi-local disorder in MHPs alloys can be analyzed from a statistical ensemble approach[30,31]. However, keeping accuracy at the ab initio approach levels might be challenging since MHPs involves the employment of relativistic corrections, such as GW approximation[32–35] or even spin-orbit coupling for the gap energy mapping[19]. In this context, protocols combining generalized quasichemical approximation (GQCA)[36] and density functional theory (DFT) were capable to reproduce near-infrared absorption spectra through Kubelka–Munk experiments to the $MAPb_{1-x}Sn_xI_3$[17,21,22,37], from which the DFT+SOC/GQCA as a theoretical approach showed how the Sn/Pb ordering in the alloy leaves a coincident maximum absorbance/red shift with the minimum energy gap[17].

Constructing a reliable statistical ensemble for mixed metal halide perovskites (MHPs) presents significant challenges, particularly when considering polymorphic contributions. The complexity and variability inherent in mixed MHP systems necessitate a robust, methodical approach. Employing automated scientific workflow frameworks may significantly enhance this process. Such frameworks offer numerous advantages: they provide a structured, repeatable methodology for handling complex simulations, facilitate comprehensive data analysis, and ensure results' reproducibility. By automating simulation protocols, these workflows efficiently manage the intricate calculations required for MHP alloys, providing a more accurate representation of their behavior in real-world conditions. This methodological rigor, enabled by automation in workflow frameworks, is crucial for advancing our understanding of MHPs alloys and their applications in various technological domains[38–40]. Here, we use an automated scientific workflow developed with the SimStack framework[38]. Our workflow allows for the nuanced modeling of $A_{1-x}Cs_xPbI_3$ (A = MA, FA) polymorphic alloys. The statistical ensemble comprehensively calculates thermodynamic properties, $T-x$ phase diagrams, optoelectronic insights, and power conversion efficiency information. This approach meticulously incorporates all critical relativistic effects, such as spin-orbit coupling (SOC) and quasi-particle corrections, underlining the efficacy of SimStack in handling sophisticated simulation protocols. Our work further demonstrates the utility of SimStack, providing a valuable tool for theorists and experimentalists. It reveals the impact of composition and polymorphic degrees on the stability and optoelectronic properties of MHP alloys. Additionally, a Colab-based notebook showcases the analysis of our raw data output, enabling users to delve into the physics of these complex problems while seamlessly managing the computational intricacies.

Results

Structural analysis of the alloys

Since the arrangements of atoms in MHP alloys are crucial for an atomistic understanding of their electronic and thermodynamic properties, we first discuss their structural parameters (i.e. lattice constants, Pb-I distances, Pb-I-Pb angles) as a function of composition and temperature. The lattice parameters calculated for each cluster configuration j associated with the $A_{1-x}Cs_xPbI_3$ (A = MA, FA) compounds are shown in Fig. 1. In this, the average values were calculated at $T = 300$ K, connecting those from $APbI_3$ (A = MA, FA; $x = 0$) to $CsPbI_3$ ($x = 1$). This temperature was selected because of experimental characterization of the alloys are usually made near room temperature[41–43]. All calculated values for the structural parameters of each j configuration associated with the polymorphs discussed here can be accessed in Supporting Information (Supplementary Tables 2–7) as numerical format.

Regarding the pure MHPs, i.e., $APbI_3$ (A = MA, FA; $x = 0.00$) and $CsPbI_3$ ($x = 1.00$), the lattice parameters calculated for all polymorphs are in good accordance with experimental reports ($MAPbI_3$[44]: 6.32 Å, $FAPbI_3$[45]: 6.36 Å, $CsPbI_3$[46]: 6.28 Å), with absolute percent deviations smaller than 3%. Because of spherical (spherical-like) nature of Cs (FA), all lattice constants for $CsPbI_3$ ($FAPbI_3$) polymorphs are nearly similar, while for $MAPbI_3$ c is greater than a and b in the $a^-a^-a^+$ configuration. This is because the C-N chemical bonds in MA cations are mostly oriented in the [100] direction, which justifies the reduction of a and b values regarding c, given the interaction of PbI_3 sublattice with MA dipole moment. However, in $a^-a^-a^-$ polymorph, the out-of-phase octahedral rotations around the apical direction (c axis) improve the coordination environment of the MA cations within the cuboctahedral cavities, leading the C-N axis of some cations to be also oriented along the [001] direction. This causes a slight expansion of a and b in this polymorph regarding $a^-a^-a^+$, with a consequent contraction of the value of c, highlighting the role of non-spherical and dipolar nature of MA in the structural properties of $MAPbI_3$ polymorphs.

By comparing FA-based alloy with its MA analog, the symmetrical-like shape of FA – whose plane containing the N-C-N bonds is nearly parallel to the equatorial direction (ab plane) in the most of supercells analyzed here – leads to $FA_{1-x}Cs_xPbI_3$ a and b lattice parameters approximately following the Vegard's law[47] in range $0.15 < x < 0.85$ for both $a^-a^-a^+$ and $a^-a^-a^-$ configurations. However, the cylindrical-like shape of MA cations makes the c values of their alloys usually higher than their a and b counterparts for $a^-a^-a^+$ polymorph since the orientation of the organic cations in the clusters is preferential with their C-N axis almost parallel to the [100] direction – similar to the pure $MAPbI_3$ system. Nevertheless, the out-of-phase octahedral rotations in $a^-a^-a^-$ polymorph leads to a suppression of the mentioned preferential orientation of MA, which is improved when increasing the Cs content in comparison with its $a^-a^-a^+$ counterpart.

In the ROT polymorph, the random octahedral rotations highlight the importance of this structural motif on the dependence of lattice parameters with the Cs content, in which we found a non-linear behavior for both $A_{1-x}Cs_xPbI_3$ (A = MA, FA) systems in the most part of compositions range. Since the linear dependence (i.e., Vegard's law) is based on the compounds having the same crystal structure[48], our results indicate that deviations from it can also occur through different stable polymorphic contributions forming the MHPs ionic networks. Following this, the value of $b > c$ is found for $MA_{1-x}Cs_xPbI_3$ ($FA_{1-x}Cs_xPbI_3$) in the range about $0.30 < x < 0.55$

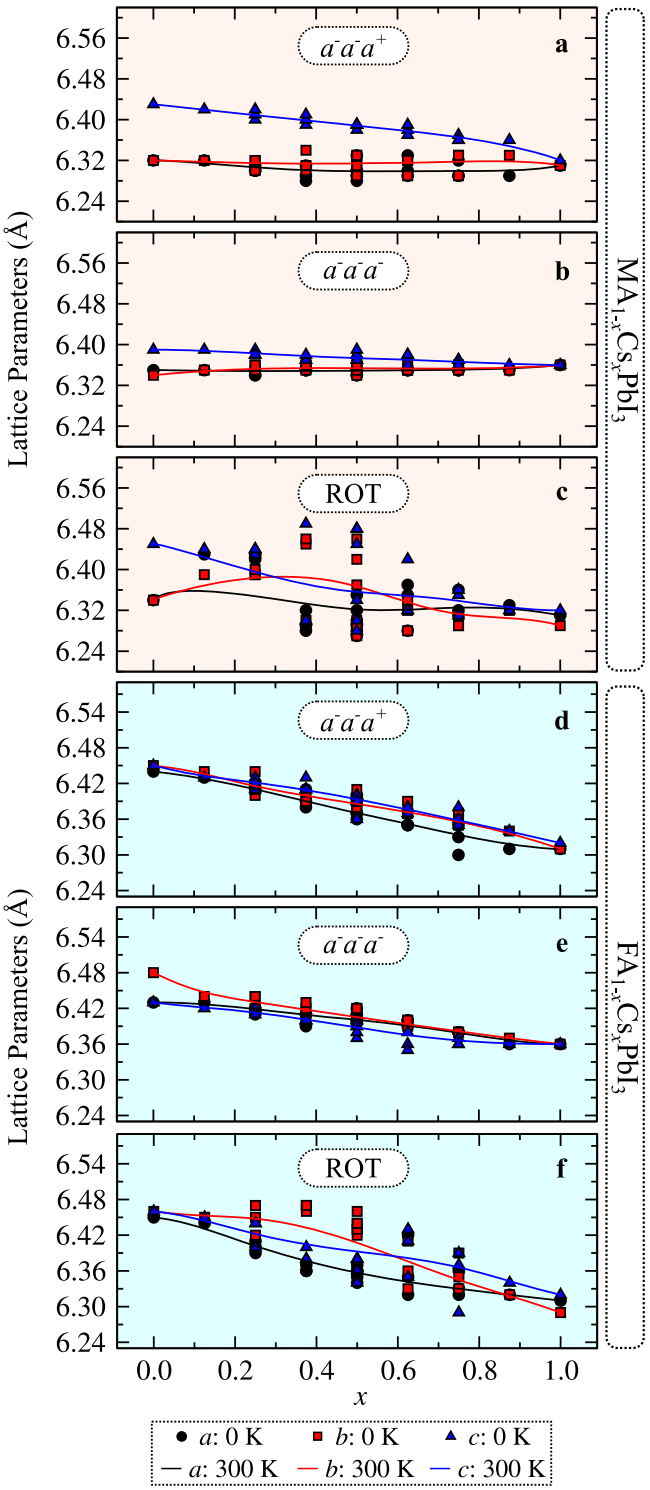

Fig. 1 | Lattice parameters. Lattice parameters calculated for clusters (scatter) and their average values (solid lines, $T = 300$ K) associated with $a^-a^-a^+$ (**a**), $a^-a^-a^-$ (**b**), ROT (**c**) polymorphs of $MA_{1-x}Cs_xPbI_3$, and $a^-a^-a^+$ (**d**), $a^-a^-a^-$ (**e**), and ROT (**f**) polymorphs of $FA_{1-x}Cs_xPbI_3$.

$(0.10 < x < 0.58)$ which is caused by a reorientation of organic molecules into the cuboctahedral cavities when increasing the Cs content.

The effects of organic-inorganic cation mixing on the Pb-I distances and Pb-I-Pb angles of $A_{1-x}Cs_xPbI_3$ (A = MA, FA) alloys are shown in Fig. 2. As a trend for the isostructural polymorphs discussed above, those based on FA cation are usually more Pb off-centering-like than their relative based on MA in compositions rich in organic cation content. This is because the higher effective ionic radius of FA (2.53 Å) in comparison to MA (2.17 Å)[49,50] induces higher local distortions in the PbI_3^- framework when fitting the space into the cuboctahedral cavities. However, when increasing the Cs content in the alloys, we found that the structure tends to become progressively on-centering-like since the difference between the shortest and longest Pb-I distance is decreased. This results from the smaller ionic radius of Cs (1.81 Å)[51] together the absence of permanent dipole moment, which causes octahedral tilts in PbI_3^- sublattice to improve the coordination environment of Cs and suppress the Pb off-center motifs. According to panels e–h, tilts are directly reflected by the difference between highest and lowest Pb-I-Pb angles decreasing from 180° for compositions with $x > 0.5$.

By comparing those local structure parameters among the polymorphs, one realizes that mixed cation alloys (i.e., $0.0 < x < 1.0$) as Glazer's pattern $a^-a^-a^-$ have the smallest distortions concerning pure MHPs at $x = 0.0$ and $x = 1.0$, while random octahedral rotations (ROT) allow the MA dipolar cations to be randomized into the cuboctahedral voids. This is explained by the organic cation interactions with the PbI_3^- framework, which induces higher Pb off-center motifs in MA-rich configurations. Grounded on that, similar findings can be made about the FA-based system.

From the results presented above, it is evident that the cation size and its dipole moment have an important influence on the local structural motifs induced in the PbI_3^- inorganic sublattice. It is important to mention that previous studies have reported the rotational activity for the methylammonium cations under finite temperature effects[52–54], at the same time, our results suggest the important role of the cations mixture in the symmetry-breaking into MHP polymorphs, which contribute as a stabilization mechanism already reported for the cubic phase[51,55,56]. Thus, composition is an additional variable with respect to the temperature to promote strong structural distortions in the cation alloys, reinforcing the necessity of a proper statistical analysis to correlate their thermodynamic stability with the structural motifs and chemical features. Below, we discuss how the polymorphic features of MHPs alloys are crucial for understanding their mixing behavior, providing insights about the preferential ordering correlated to the thermodynamic stability of the solid solutions, is analyzed here.

Themodynamic behavior of alloys

Based on the probabilities (x_j) obtained via GQCA approach, we calculated the mixing internal energies (ΔU_{mix}) throughout 100, 300, 500, 800 K temperatures from the respective excess energies ($\Delta\varepsilon_j$) according to Eqs. (2) and (3), respectively. The results are presented in Fig. 3, in which ΔU_{mix} represents the internal energies for the mixture formation and $\Delta\varepsilon_j$ is the energy of formation which identifies the stability of the structural ordering of j-th cluster regarding as reference the $APbI_3$ (A = MA, FA) and $CsPbI_3$ pure MHPs. The SOC effects on the $\Delta\varepsilon_j$ can be verified in Supplementary Fig. 3, which is usually small. In Fig. 3(a and d) (b and e), $\Delta\varepsilon_j$ was calculated for $a^-a^-a^+$ ($a^-a^-a^-$) regarding E_{APbI_3} and E_{CsPbI_3} in the same Glazer's configuration – which was named here as the Glazer's isostructural limit of the alloys. In addition, panels c and f present the results for the ROT, being completely heterostructural polymorph regarding octahedral rotations. All numerical $\Delta\varepsilon_j$ values calculated for these contributions are also presented in Supplementary Tables 8–13. Furthermore, we also considered the effect of all these polymorphs together through the APD statistics, in which $\Delta\varepsilon_j$ values were calculated by using the E_{APbI_3} and E_{CsPbI_3} from their most stable configuration, i.e., $a^-a^-a^+$, as shown in Fig. 4.

In the Glazer's isostructural limit of alloys, most of the j associated with $a^-a^-a^-$ polymorph (panels b and e) presented negative excess energies, which indicates that both $FA_{1-x}Cs_xPbI_3$ and $MA_{1-x}Cs_xPbI_3$ mixed MHPs usually tend to be more stable than the $APbI_3$ and $CsPbI_3$ in this polymorph[15]. This is in accordance with the $a^-a^-a^-$ showing mixed j with the lowest differences regarding the Pb-I-Pb angles in their pure $APbI_3$ counterparts, in which the replacement of A = MA and FA by Cs as spherical-like cation is energetically favorable into the $a^-a^-a^-$ yielding a low symmetry cavity (Fig. 2e, k). However, for the $a^-a^-a^+$ polymorph (panels a and d), we found that most of the j presented positive excess energies, with an energetically favored one showing $\Delta\varepsilon_j = -5.63$ meV per cation

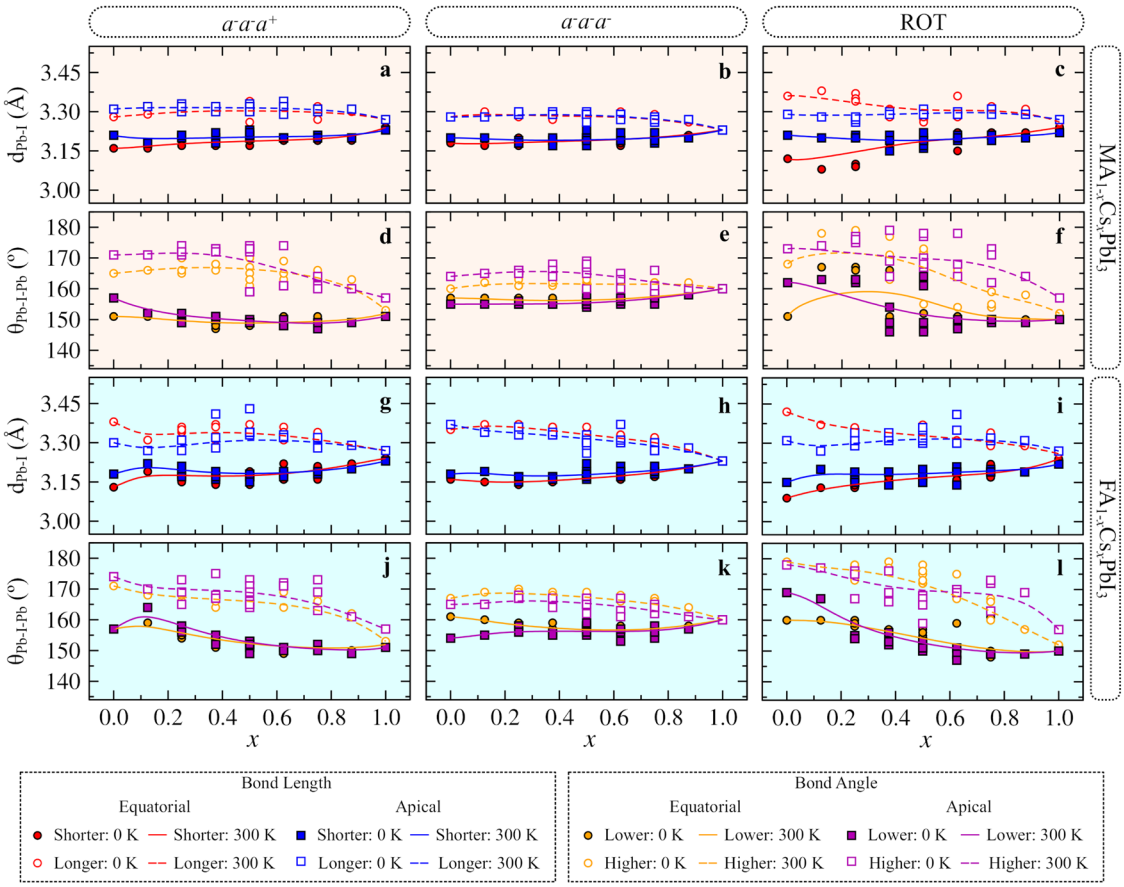

Fig. 2 | Cluster distances. Shortest/longest Pb-I distances (**a**–**c**, **g**–**i**), and highest/lowest Pb-I-Pb angles (**d**–**f**, **j**–**l**) along the equatorial (Equat., *ab* plane) and apical (Api., *c* axis) directions, calculated for clusters (scatter) and their average values (solid and dashed lines, $T = 300$ K) for $a^-a^-a^+$, $a^-a^-a^-$ and ROT polymorphic contributions for $A_{1-x}Cs_xPbI_3$ (A = MA, FA) alloys.

($\Delta\varepsilon_j = -17.65$ meV per cation) for MA (FA) based alloy at $x = 0.625$ ($x = 0.125$). This is closely related to a tendency to form long-range ordered compounds at the referred compositions when energy effects predominate over the entropic ones[16], in which the stabilities are achieved through the complete immersion of the inorganic cations (rows of Cs cations along [001] and [010] directions) in the matrix of organic cations (intercalated MA-Cs rows along [001] and [010] directions) for $FA_{1-x}Cs_xPbI_3$ ($MA_{1-x}Cs_xPbI_3$) – see Supplementary Fig. 4 in Supporting Information. This interpretation also is applied to ROT results (panels c and f), given the presence of in-phase Glazer's rotations in PbI_3^- sublattice becomes less favorable for the alloys than $APbI_3$ pure MHPs in this isostructural Glazer's limits.

The thermodynamic description of the alloys in the isostructural Glazer's pattern is limited. Since j_s with $a^-a^-a^+$ pattern are usually thermodynamically favored to the detriment of their $a^-a^-a^-$ relatives, we highlight the limitations of isostructural modeling of MHPs alloys in Fig. 4, in which the origin of miscibility gaps at low temperatures for the materials analyzed here[57] could also be correlated with the presence of out-of-phase octahedral rotations in their respective PbI_3^- sublattice. This is because $a^-a^-a^-$ pattern suppress the Pb off-center motif and present both shorter and longer Pb-I-Pb angles near to each other, changing the cuboctahedral voids topology and, consequently, hindering the cation accommodation into their respective coordination environment. For instance, in ROT by considering FA with a higher effective radius (2.53 Å) than Cs (1.81 Å), distortions in the PbI_3^- sublattice regarding $FAPbI_3$ ($CsPbI_3$) in the $a^+a^+a^+$ ($a^-a^-a^+$) configuration allows a reduction of strain to accommodate the cations inside better the cuboctahedral cavities. Because of the smaller size of MA regarding FA, Pb-I-Pb angles closest to 180° in ROT reduces its effective coordination by the PbI_3^- framework, making $\Delta\varepsilon_j$ as high as 53 me V per cation by taking $MAPbI_3$ ($CsPbI_3$) in the $a^-a^-c^-$ ($a^-a^-a^+$) configuration as a reference for the corresponding pure MHPs.

Because miscibility gaps are possible to occur in A-cation MHP alloys at room and higher temperatures[6,57–59], we discuss their thermodynamic stability by using their respective mixing-free energies (ΔF_{mix}) as a function of temperature and composition, whose results are depicted in Fig. 5. The associated configurational entropies (ΔS_{mix}) are presented in Supplementary Fig. 5. Since the thermodynamic description of the alloys in the isostructural Glazer's pattern is limited, we focus on the APD only, and discussions about the individual polymorphs can be accessed in Supporting Information (Supplementary Fig. 6, Section VII).

Our findings concerning the collective contributions involving cation mixture and polymorphic effects – as an average over a polymorphic ensemble alloy – are confirmed by experiments, from which $FA_{1-x}Cs_xPbI_3$[57] reach a higher stability for FA excess. Therefore, all the polymorphs considered above as an isostructural Glazer's pattern configuration can be interpreted as a function of T. This can be understood by observing the probabilities of each polymorph contributing to APD systems, whose values are shown in Fig. 6 at different temperatures. Since increasing T allows higher energy (metastable) configurations to be accessed by pure MHPs, their energy references will vary concerning the most stable Glazer configuration at $T = 0$ K (i.e., $a^-a^-a^+$), with the stability of solid solutions regarding the pure MHPs being analyzed from a convex hull-like perspective[60].

In more details, our calculated polymorph probabilities (x_k) reveal that at temperatures in range 100–800 K both MA and FA-based alloys are mainly formed by a mixing of j_s from $a^-a^-a^+$ and ROT polymorphs. However, the probability associated with those from their $a^-a^-a^-$ relatives increases when the temperature is raised. Interestingly, when looking at the

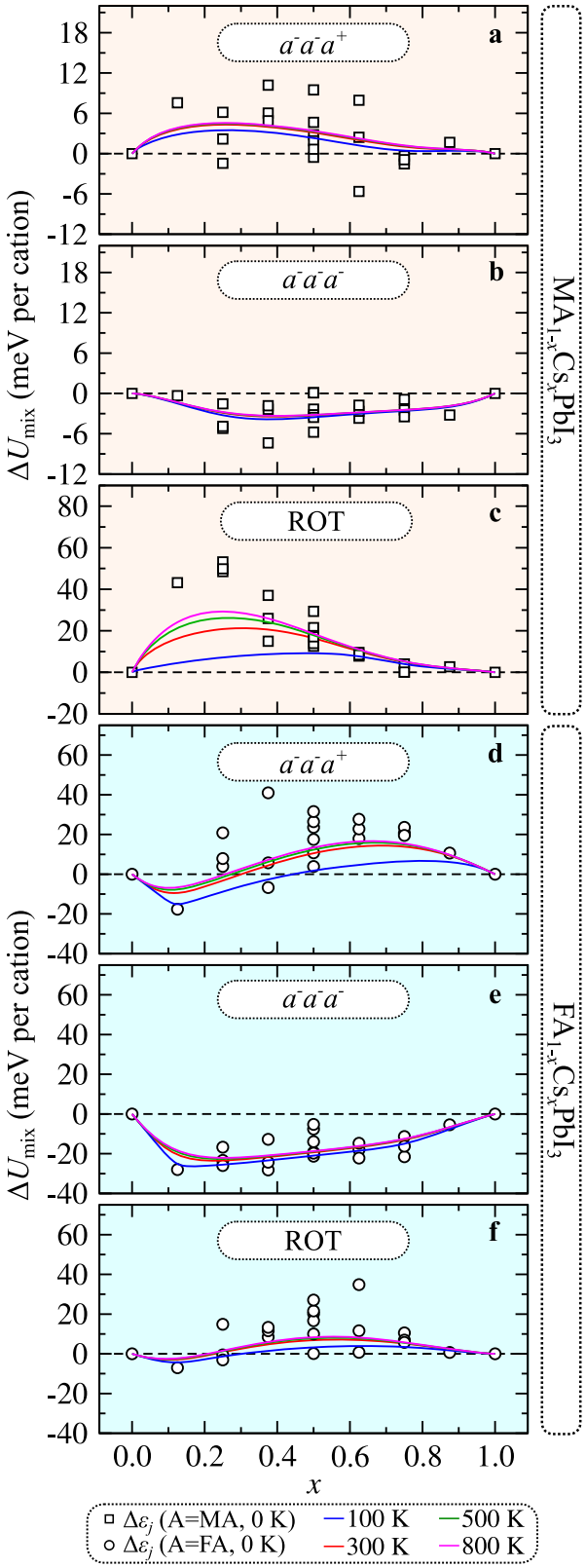

Fig. 3 | Cluster excess energies. Excess energies ($\Delta\varepsilon_j$, scatter) calculated for the each j cluster expanding the $MA_{1-x}Cs_xPbI_3$ (**a**–**c**) and $FA_{1-x}Cs_xPbI_3$ (**d**–**f**) alloys and their respective ΔU_{mix} (solid lines) from 100 to 800 K.

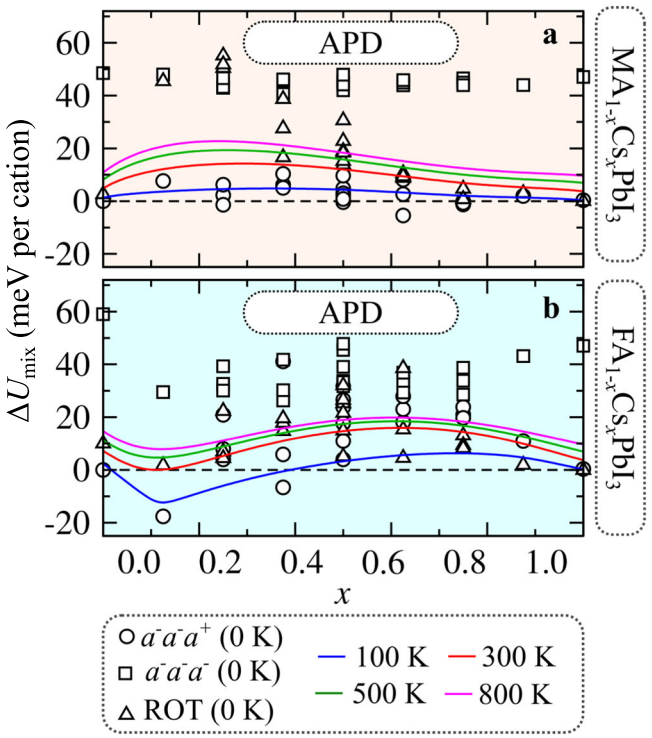

Fig. 4 | Cluster excess energies calculated via APD. Excess energies ($\Delta\varepsilon_j$, scatter) calculated for the each j cluster expanding the $MA_{1-x}Cs_xPbI_3$ (**a**) and $FA_{1-x}Cs_xPbI_3$ (**b**) alloys and their respective ΔU_{mix} (solid lines) from 100 to 800 K calculated via APD statistics.

FA-based system, ROT tends to be favored in Cs-compositions, while $a^-a^-a^+$ in those where the organic cation is predominant. This occurs because distortions of the PbI_3^- sublattice in ROT allows for reduction of the strain in accommodating the large FA in the Cs-rich matrix, while the adjust of Cs in a FA-rich matrix is favored when the $a^-a^-a^+$ Glazer's the pattern is present. Thus, the alloy tends to order in different polymorphs at low temperatures, i.e., the former in $a^-a^-a^+$ and the latter with ROT, showing the ordering polymorphic pattern as being a direct the function of the alloy composition, which is also supported by Supplementary Fig. 11.

Phase diagrams of alloys

To provide insights about the effects of polymorphic contributions on alloys' stability and metastability as a function of the temperature and composition, we calculate their isobaric T-x phase diagrams[61]. The results are shown in Fig. 7, with the T_c values being highlighted by dashed lines.

Panels a–c show that for $MA_{1-x}Cs_xPbI_3$ system, a higher tendency to phase segregation in x region associated with MA-rich systems is obtained below T_c, with stable solid solutions being found for all temperatures only above $x = 0.58$ for APD alloy. As indicated by $\Delta\varepsilon_j$ values (Fig. 4a), it is more energetically unfavorable to add Cs into a MA-rich matrix, since this leads to a break of local electrostatic interactions between neighboring MA dipole moments and the PbI_3^- inorganic framework, revealing the role of the MA dipole moments on the thermodynamic stability of the cation MHP alloys. Above T_c, the entropic effects dominate over the energetic ones, and the alloy is stable for all compositions.

Our results indicate that the presence of random octahedral rotations in the alloy, which mimics the effect of local fluctuations in the structure at higher $T > 0$ K, are responsible to increase the critical temperature for $MA_{1-x}Cs_xPbI_3$ system, given the huge T_c value found in panel b. However, when they are brought together with the other polymorphic contributions in APD, this effect is considerably reduced, since the clusters from $a^-a^-a^+$ polymorph are statistically favored to the detriment of the ROT ones (see Fig. 6).

In the case of $FA_{1-x}Cs_xPbI_3$, the segregation preferentially occurs at Cs contents higher than $x = 0.20$, with a completely unstable solid solution between $x'_a = 0.34$ and $x'_b = 0.81$ at $T = 300$ K for APD. Since the magnitude of FA dipole moment (0.25 D) is smaller than its MA relative

(2.15 D)[62], steric effects play a more fundamental role regarding the thermodynamic stability of this system as a solid solution and its phase segregation. Because FA is about 40% higher than Cs[49–51], its incorporation in a Cs-rich matrix is more thermodynamically unfavorable when compared with the opposite situation, since higher strain is induced in the alloy lattice in the former for the $a^-a^-a^+$ polymorphic configuration, which present higher x_k contributions for APD at 300 K. Afterward random octahedral rotations allow to reduce this strain, T_c is lowered in panel e in comparison with d, in correlation with x_k of ROT clusters being more likely at higher Cs-contents in APD. These findings are in good accordance with experimental reports, which suggest the limit for Cs content in the cubic phase of $FA_{1-x}Cs_xPbI_3$ to be about 15–20% at room temperature, and the bulk $FA_{0.9}Cs_{0.1}PbI_3$ compound being synthesizable and stable at 300 K[10,58,59,63]. Furthermore, experimental solid solutions at room temperature with x between 0.25–0.30 were demonstrated to suffer phase segregation after 20 h on light exposition, with the appearance of two $FA_{1-x}Cs_xPbI_3$ segregated phases with $x \approx 0.20$ and $x \approx 1.00$, respectively. In addition, nominal $FA_{0.65}Cs_{0.35}PbI_3$ and $FA_{0.6}Cs_{0.4}PbI_3$ demonstrated phase segregation after a short time exposure under light, while $FA_{0.85}Cs_{0.15}PbI_3$ and $FA_{0.8}Cs_{0.2}PbI_3$ compounds presented good stability, with no phase segregation even after being continuously irradiated for 100 h, in good correlation with the APD phase diagram presented in Fig. 7 f[57].

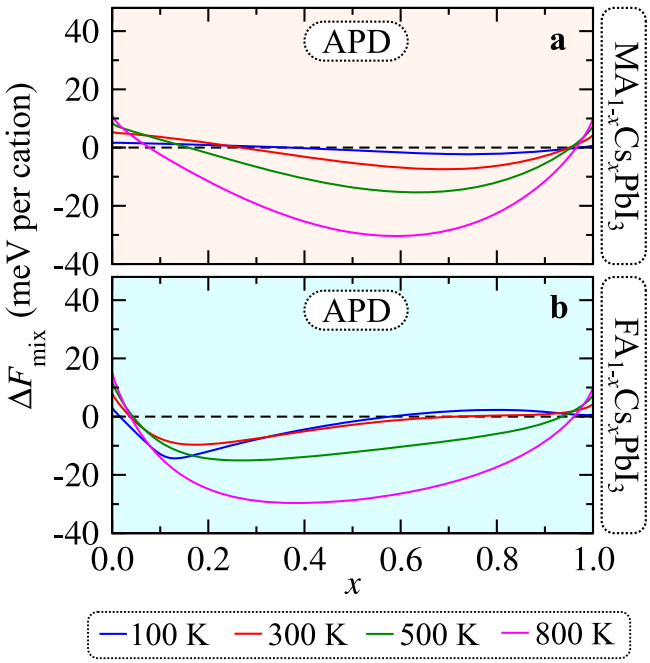

Fig. 5 | Mixing free energies as a function of the alloy composition and temperature. For $MA_{1-x}Cs_xPbI_3$ (**a**) and $FA_{1-x}Cs_xPbI_3$ (**b**) by considering all polymorphic degrees (APD).

Gap energies of alloys from DFT-1/2+SOC protocol

To map out the polymorphic features on the gap energies (E_g) of the $MA_{1-x}Cs_xPbI_3$/$FA_{1-x}Cs_xPbI_3$ compounds, we compute their average values over a range of compositions through GQCA approach. Figure 8 depicts the results obtained by employing the DFT-1/2+SOC protocol[14,19,64], in which yellow filled symbols indicate experimental reports. The energy gaps calculated for all individual clusters used to construct our structural ensemble can be found in Supporting Information (Supplementary Tables 14–19) and the ones obtained via standard DFT and DFT+SOC approaches.

In panels a and c, gap energy curves with different signatures are present, depending directly on the particular Glazer's pattern involved. Details about them are discussed in Supporting Information. Here we focus on APD since, as highlighted above, the isostructural approach is limited. Thus, when we put together all the effects of individual polymorphs considering APD, an excellent agreement was obtained between the values calculated through the GQCA and their experimental counterparts. As shown in Fig. 8b, d, the latter are all within the shaded regions associated with the statistical error of averaged values, evidencing the importance of polymorphic degrees conferring to the cation alloys their experimentally measured properties, in line with our previous works about pure MHPs as polymorphous networks[14,19,64]. In addition, our results here also evidence the importance of statistical protocols in the alloys treatise from an ab initio perspective, since only the analysis of gap energies cannot allow distinguishing between the different polymorphic contributions to each alloy. As shown in Fig. 6, the cation nature directly impacts the polymorphic character in APD as a function of composition, in which only the gap analysis does not allow to distinguish between $a^-a^-a^+$ and ROT for $FA_{1-x}Cs_xPbI_3$ ($MA_{1-x}Cs_xPbI_3$) in $x > 0.7$ ($x > 0.8$), while the $a^-a^-a^-$ being the high energy polymorphic contribution have minor statistical contributions for the alloys.

Optical properties and PCE via GQCA

By applying the SLME model with the DFT-1/2+SOC protocol, we estimated the influence of polymorphic features on the alloys' performance in solar cells by calculating their PCE values via GQCA ensemble averages. The results as a function of x at room temperature ($T = 300$ K) are shown in Fig. 9. The absorption coefficients (α) calculated at the most favorable composition in this temperature (i.e., at x corresponding to the minima of $\Delta F_{mix}(x, 300\ K)$ profiles in Fig. 5 and Supplementary Fig. 6) are available in Supplementary Fig. 14.

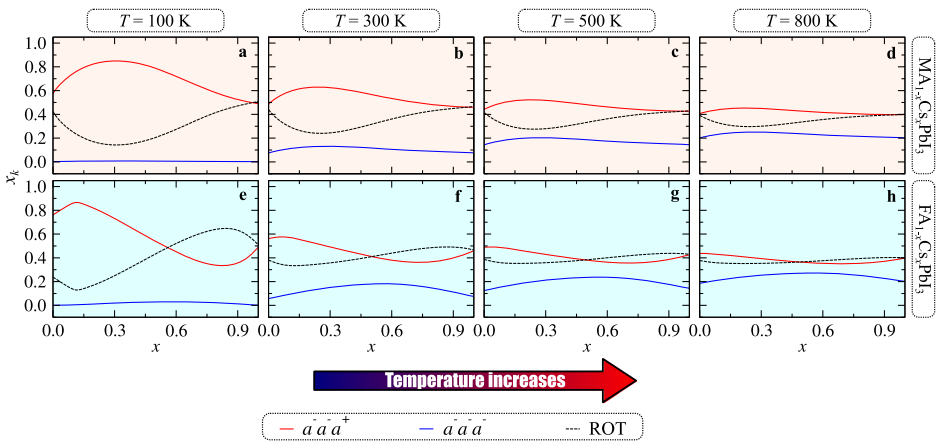

Fig. 6 | Polymorph probabilities. Polymorph probabilities in the function of composition at T in range 100–800 K for $MA_{1-x}Cs_xPbI_3$ (**a**–**d**) and $FA_{1-x}Cs_xPbI_3$ (**e**–**h**) considering all-polymorphic degrees (APD) from their $\boldsymbol{a^-a^-a^+}$ (red), $\boldsymbol{a^-a^-a^-}$ (blue) and ROT (black) polymorphs.

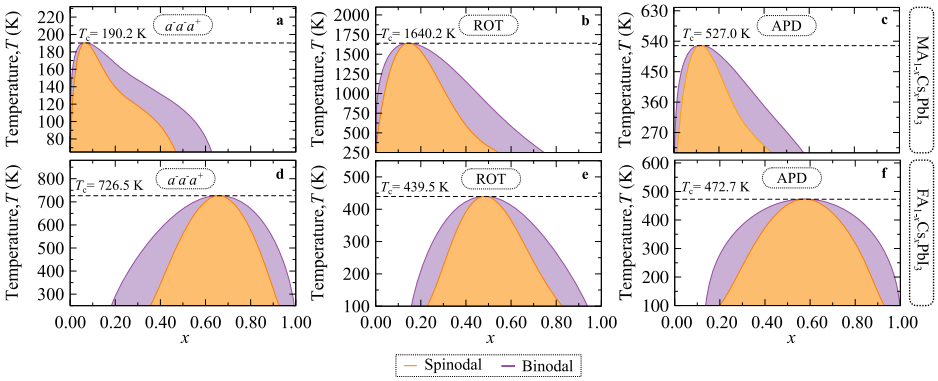

Fig. 7 | Phase diagram. Calculated phase diagram for $MA_{1-x}Cs_xPbI_3$ in the $a^-a^-a^+$ isostructural polymorph (**a**), ROT polymorph (**b**), and all-polymorphic degrees (APD) (**c**) and for $FA_{1-x}Cs_xPbI_3$ in the $a^-a^-a^+$ isostructural polymorph (**d**), ROT polymorph (**e**), and all-polymorphic degrees (APD) (**f**). The metastable and unstable states are associated with purple and orange regions enclosed by the binodal and spinodal lines. The white regions correspond to thermodynamically stable solid solutions. Critical temperatures (T_c) are highlighted using dashed lines in the graphs.

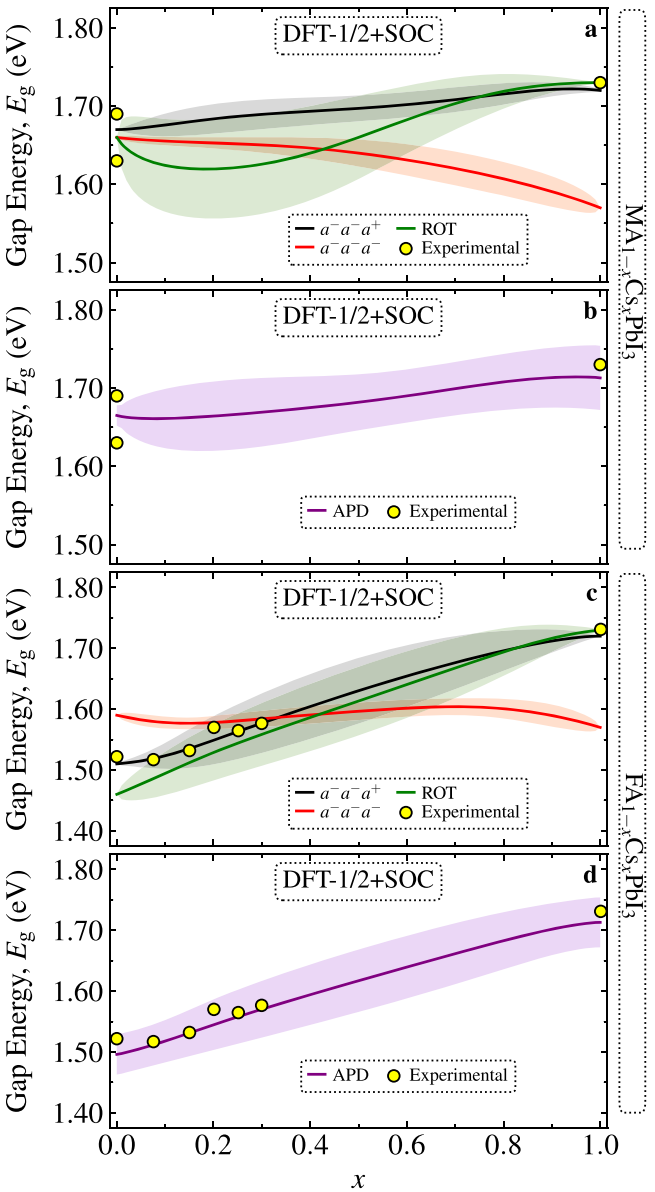

Fig. 8 | Gap energy. Gap energy (E_g) in function of composition at $T = 300$ K for $MA_{1-x}Cs_xPbI_3$ (**a**, **b**), and $FA_{1-x}Cs_xPbI_3$ (**c**, **d**), in $a^-a^-a^+$ (black), $a^-a^-a^-$ (red), ROT (green) and APD (purple) polymorphs. Shaded regions indicate the standard deviation of averaged values calculated within the GQCA statistical approach. Experimental results, when available, are indicated by yellow circle symbols[26,92,93].

As a general trend, the PCE values calculated for both $A_{1-x}Cs_xPbI_3$ alloys follow the behavior of gap energies shown in Fig. 8, where compositions with lower E_g values present higher PCE ones in both isostructural and APD limits. Thus, PCEs in Fig. 9b, d are dominated by the polymorph with the highest probability at 300 K (Fig. 6), being $a^-a^-a^+$ for MA-based system in $0.0 < x < 0.90$ while for FA-based one it corresponds to $a^-a^-a^+$ for $0.0 < x < 0.50$ and ROT for $0.50 < x < 1.00$.

A complete overview of the alloys analyzed here is provided by correlating their gap energy, composition, and total absorption coefficients ($\sum_\alpha$) through their APD GQCA statistics, as shown in Fig. 10. For $MA_{1-x}Cs_xPbI_3$ system (panel a), we verified that $\sum_\alpha$ tends to decrease for all compositions in comparison with $MAPbI_3$, even though the E_g values for $0.00 < x < 0.10$ are a little lower than their pristine $APbI_3$ (A = MA, Cs) correspondents. This compensatory effect between E_g and $\sum_\alpha$ reduction correlates with the PCE of the alloy not being significantly changed in this range of compositions when compared to that of $MAPbI_3$ (see Supplementary Fig. 15). However, since the alloy is mostly metastable or unstable in this region (Fig. 7c), the reduction in total absorption and the increase in E_g for $x > 0.50$ culminates in a reduction of less than 1% in PCE, suggesting that Cs-rich solid solutions based on $MA_{1-x}Cs_xPbI_3$ would still be good candidates for application in solar cells.

Regarding $FA_{1-x}Cs_xPbI_3$ system (panel b), due to a stronger dependence of E_g on the alloy composition, $\sum_\alpha$ stay with values higher than 13.5% for $0.00 < x < 0.30$, with PCE varying less than 1% in comparison with $FAPbI_3$ only about $0.00 < x < 0.10$ (Supplementary Fig. 14). Thus, the results point out for FA-rich $FA_{1-x}Cs_xPbI_3$ alloys as the best candidates for photovoltaic applications with the highest PCE values since the latter composition range is thermodynamically stable when $T > 300$ K.

Discussion

Here, we proposed an automated Workflow approach to analyze the thermodynamic stability, statistical attributes, and electronic properties of MHPs cation alloys. Because of the polymorphous features of these materials, protocols using only one type of structural motif regarding the Glazer's rotations, cation configurations, and the corresponding local symmetry breakings cannot capture the complete physical behavior of these systems. This is evident when we compare the corresponding values obtained for the critical temperatures for individual polymorphs and consider both contributing to the perovskite structure. Our approach also quantified polymorph probability in the alloys. In addition, the protocol proposed here allowed to obtain gap energies in excellent agreement with the available experimental reports, reflecting the statistical nature of the MHPs alloys both from the A-cation configurational disorder and the disorder from the polymorphic nature intrinsic to the MHPs. Thus, joining together the statistical features of GQCA with the SLME model, we computed the corresponding PCEs of $A_{1-x}Cs_xPbI_3$ *in operando* conditions of temperature, in direct connection with their main application in solar cells devices under optimized compositions.

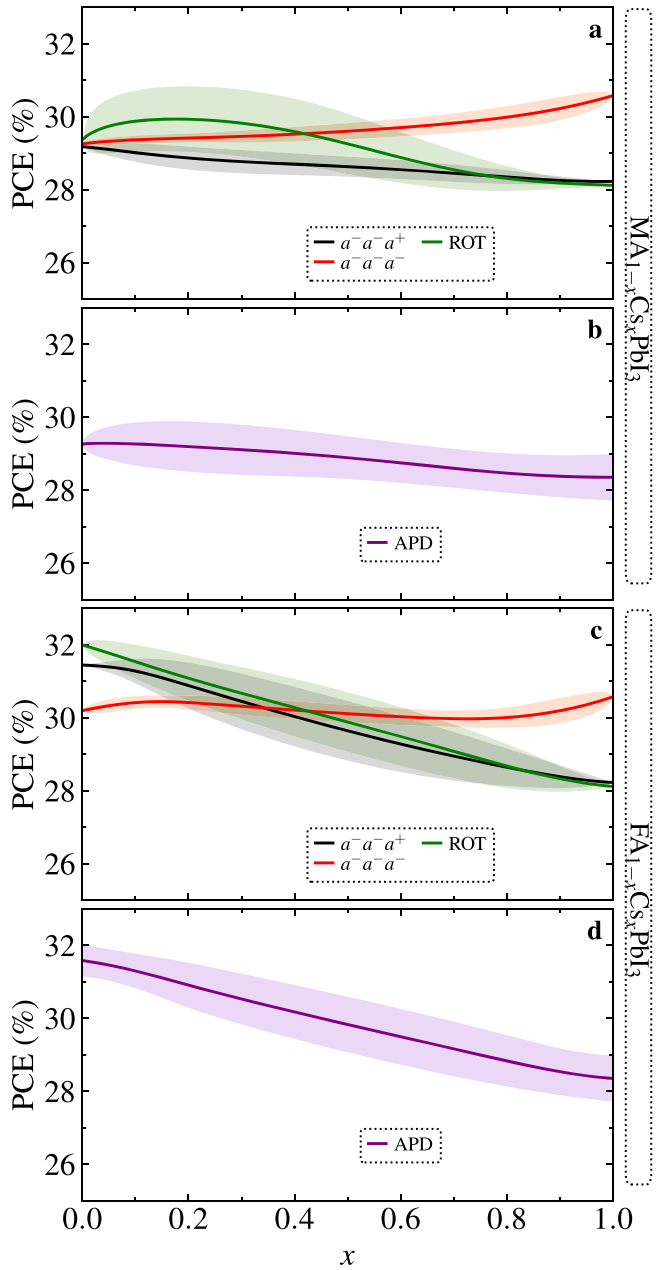

Fig. 9 | Power conversion efficiency. Calculated power conversion efficiency (PCE) for $MA_{1-x}Cs_xPbI_3$ in the $a^-a^-a^+$, $a^-a^-a^-$, ROT (**a**), and all-polymorphic degrees (APD) (**b**), and for $FA_{1-x}Cs_xPbI_3$ in the $a^-a^-a^+$, $a^-a^-a^-$, ROT (**c**), and all-polymorphic degrees (APD) (**d**) by applying the SLME model via GQCA statistics.

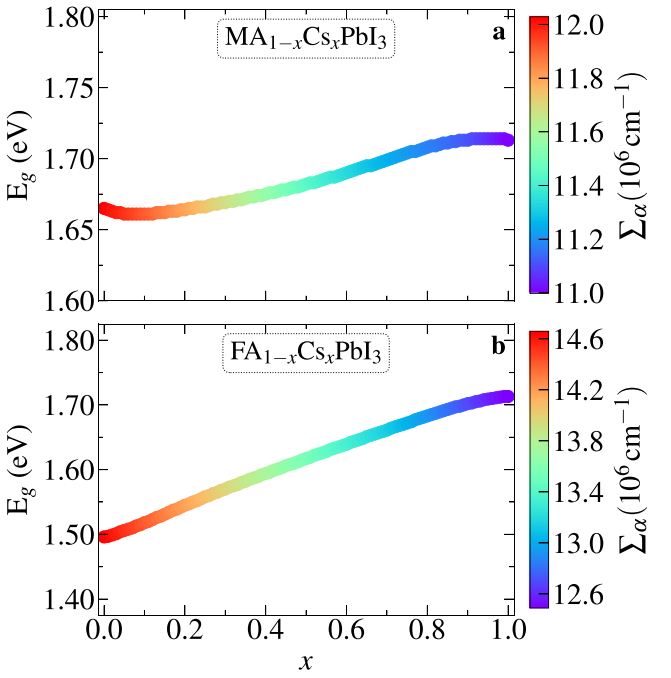

Fig. 10 | Correlation. Correlation between the gap energy, composition and total absorption coefficients ($\sum_\alpha$) calculated through GQCA at 300 K for $MA_{1-x}Cs_xPbI_3$ (**a**) and $FA_{1-x}Cs_xPbI_3$ (**b**) by considering APD as the alloy's ensemble. The color map corresponds to the $\sum_\alpha$ obtained via GQCA ensemble statistics for the photon energy range 0.0–4.0 eV.

As summary, we performed a systematic first-principles investigation about the polymorphic features of $A_{1-x}Cs_xPbI_3$ (A = MA, FA) pseudo-cubic alloys, analyzing the impact of mixing organic and inorganic cations on their structural and electronic properties, configurational disorder and thermodynamic stability. Through an automated cluster expansion within the generalized quasichemical approximation, as implemented in SimStack and Colab platforms, our results indicate that both the effective radius of organic cation and its dipole moment impacting the Glazer's pattern in the PbI_3^- sublattice have an essential role on the alloys stabilization and phase segregation. Because $a^-a^-a^+$ polymorph is the most stable contribution for both alloys, the positive excess energies for $a^-a^-a^-$ when considering APD indicate that the origin of miscibility gap in polymorphic alloys can be correlated with the presence of out-of-phase Glazer's contributions in their respective PbI_3^- inorganic framework, pointing out that isostructural limit of alloys is a limited approach and cannot reveal the complete physical behavior behind their thermodynamic, structural and electronic properties. Therefore, the phase diagrams calculated considering the APD statistics correlated well with the experimental findings on the stability of the systems analyzed here, allowing to detail how different polymorphic contributions can stabilize and change their respective values of T_c. Thus, a breakthrough was obtained in the rational design of thermodynamically stable MHPs cation alloys, which can be used to optimize PSCs in their most diverse operating temperature conditions. We also highlight future works to which our protocol can be applied, such as the study of the thermodynamic stability of fully inorganic cation alloys in the A-site ($A_{1-x}Cs_xPbI_3$, A = Na, K, Rb), Pb-free MHPs alloys such as $A_{1-x}Cs_xSnI_3$, $A_{1-x}Cs_xGeI_3$ (A = Na, K, Rb, FA, MA) or even mixed solutions between inorganic halide ($CsBX_3$, B = Ge, Sn, Pb; X = Cl, Br, I) and oxide-based perovskites ($SrBO_3$, B = Rh, Ti), whose extension, based on our SimStack workflow, is made simple.

Methods

Automation procedures through the simstack framework

We generated the raw data by employing a Workflow Active Nodes (WaNos) set within the SimStack framework[38], as illustrated in Fig. 11. The data flow originated from a statistical ensemble created using a variety of representative configurations for metal halide perovskite (MHP) alloys. The generated data is readily accessible on our GitHub repository (https://github.com/Alloys-Workflow). This dataset was produced through the integration of five distinct WaNos. Additionally, a Colab notebook facilitates the extraction of average properties across the MHP alloys ensemble. Below, we describe and show our automated workflow designed to determine average thermodynamic and optoelectronic properties for a statistical ensemble of polymorphic $MA_{1-x}Cs_xPbI_3$ and $FA_{1-x}Cs_xPbI_3$ alloys:

SOD-2022. Our protocol identifies a set of equivalent configurations to represent the cation MHPs alloy ensembles accurately. Utilizing the cluster expansion framework, we adopted a set of supercells as our basis. This approach, referenced in multiple studies[16,36,65,66], ensures that each

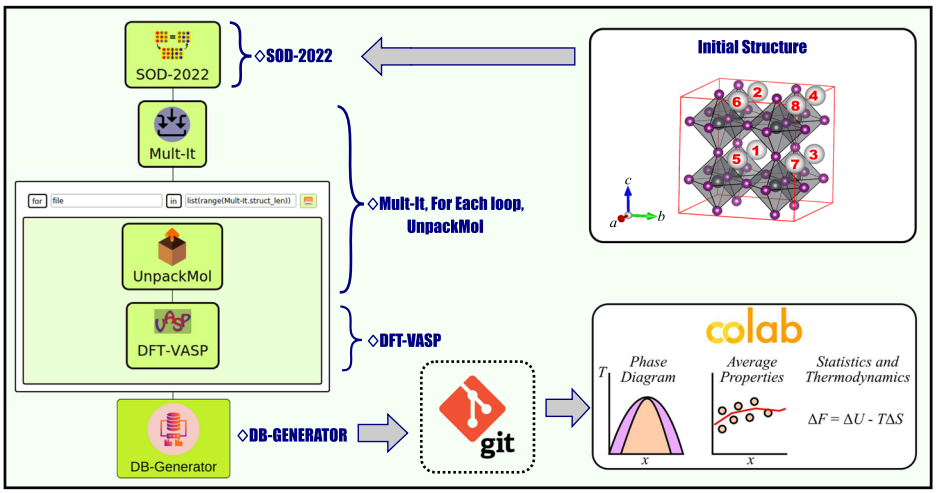

Fig. 11 | SimStack workflow. This illustration depicts the comprehensive SimStack workflow employed for calculating the properties of semiconductor alloys using the Generalized Quasi-Chemical Approximation (GQCA) protocol.The workflow integrates a series of WaNos: SOD-2022, Mult-It, UnpackMol, DFT-VASP, and DB-Generator. Each WaNo plays a specific role in the process: SOD-2022 generates cluster configurations and their degeneracy factors. Mult-It: facilitates the creation and management of data lists. UnpackMol: prepares configuration files for DFT analysis. DFT-VASP: conducts Density Functional Theory calculations. DB-Generator: compiles the results into a database. Additionally, the workflow leverages the capabilities of GitHub, connecting the data set generated via workflow with a Colab notebook for phase-diagram analysis and determining average, statistical, and thermodynamic properties of metal halide perovskite (MHP) alloys.

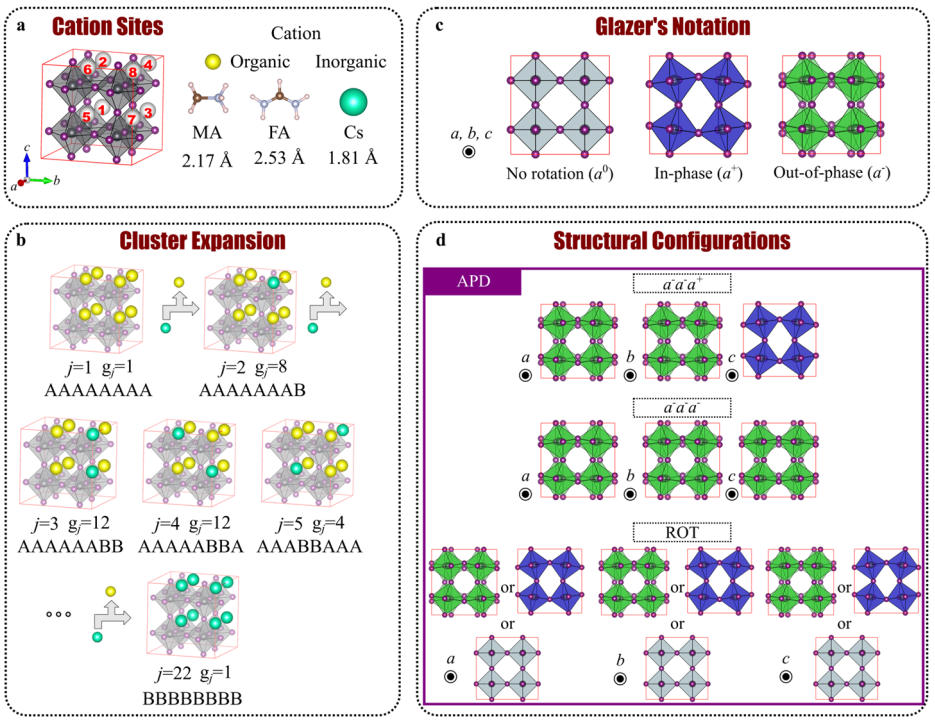

Fig. 12 | Structures. a Pictorial representation of the $APbI_3$ ($CsPbI_3$) $2 \times 2 \times 2$ supercell expansion. The cuboctahedral sites are numbered from 1 to 8, in which the organic cations (A = MA, FA) are replaced by Cs to built the MHPs alloys. **b** Alloy cluster expansion schematization. The organic cations are depicted as yellow spheres, and the inorganic ones are turquoise spheres. The gray arrows indicate the substitution of organic cations by Cs. **c** Glazer's notation schematization, with a^0 representing no rotation, a^+ in-phase rotation, and a^- out-of-phase rotation. **d** Picture of structural configurations of alloys, with Glazer's rotations around each a, b and c cell axis (pointing out of the paper plane) in $a^-a^-a^+$, $a^-a^-a^-$, ROT and APD (all configurations together) being showed.

supercell is statistically and energetically independent. Specifically, we expanded a $2 \times 2 \times 2$ supercell from a cubic unit cell, starting with $MAPbI_3$ (or $FAPbI_3$) as the parent MHPs, as depicted in Fig. 12a[16,17]. Subsequently, the alloys were engineered by substituting MA (FA) cations with Cs in eight cuboctahedral sites. This process resulted in cluster configurations representing $MA_{1-x}Cs_xPbI_3$ ($FA_{1-x}Cs_xPbI_3$) solid solutions, schematically illustrated in Fig. 12b. In these configurations, A labels the organic cations, and B denotes the inorganic ones, following the sequence 12345678 in panel a. Treating each cation mixed MHP as a pseudobinary alloy, the two cation options at the cuboctahedral sites yield $2^8 = 256$ configurations. However, symmetry operations within the cubic $Pm\bar{3}m$ macroscopic space group categorize these into $J = 22$ classes of equivalent configurations. Each class has its specific degeneracy factor (g_j), as shown in Fig. 12b and Supplementary Table 1 in the Supplementary Material. The SOD program facilitated the generation of all these degeneracy factors and structures[31], as integrated into the SOD-2022 WaNo in the SimStack workflow. Since SOD is based on symmetry operations of the corresponding structure, the SOD-2022 WaNo can be applied for MHPs alloys with any spacegroup, which is also extendable to other types of (pseudo)binary alloys beyond MHPs.

To capture the polymorphic nature associated with MHPs investigated here, we considered their octahedral tilts, Pb metal off-center displacements

within octahedra, and positional rearrangements of cations into the cuboctahedral voids of clusters. The former were denoted by using the Glazer's notation[67], in which strings are associated with the magnitude (a, b or c), and superscripts with the relative orientation (e.g., a^0 for no rotation, a^+ in-phase, and a^- out-of-phase) of the octahedra rotations along each direction parallel to the crystal axis of our (pseudo)cubic cells, as depicted in Fig. 12c. More details can also be accessed in Supporting Information (Supplementary Fig. 1).

We have considered our previous studies regarding the thermodynamic stability of $CsPbI_3$[14] through the $CsI(s) + PbI_2(s) \longrightarrow CsPbI_3(s)$ synthesis route, in which polymorphic effects were captured. According to this, two Glazer's configurations were chosen to verify the effects of octahedral rotations on the thermodynamic and electronic properties of our alloys, respectively, $a^-a^-a^+$ ($\Delta_f H = -116$ me V per cation) and $a^-a^-a^-$ ($\Delta_f H = -81$ me V per cation), which present relative energies of -96 me V per cation and −62 me V per cation, respectively, regarding the $a^0a^0a^0$ rotation pattern. This was named the alloy's isostructural limit.

We also evaluated the impact of random octahedral rotations on alloy properties. Specifically, we introduced slight positional adjustments to all atoms within the clusters before optimization. This process called random octahedral tilts (ROT), does not follow any predefined octahedral rotation pattern. Moreover, we investigated the combined effects of several structural motifs on the alloys' thermodynamic stability. The resulting statistical analysis of the alloys incorporates all these polymorphic contributions. It is termed the all polymorphic degrees (APD) approach. This approach is symbolically represented by the combination of $a^-a^-a^+ + a^-a^-a^- + \mathrm{ROT}$. The APD methodology extends the principles of generalized ensemble formalism, traditionally used in modeling alloys with clusters from different crystal structures[15]. However, in our case, we focus on analyzing a cubic crystal structure enriched with multiple polymorphic elements. Consequently, the set of configurations we explored is outlined as follows:

- $a^-a^-a^+$: stablest isostructural limit;
- $a^-a^-a^-$: metastable isostructural limit;
- ROT: random octahedral tilts;
- APD: all polymorphic degrees.

A schematic representation of each configuration set is presented in Fig. 12d.

Mult-It. The Mult-It WaNo streamlines the generation of lists and data management within our workflow. With this tool, effortlessly create lists of both floats and integers and conveniently read lists of file names. Specifically, it aids in quickly generating the required lists and reading file names from .tar files. This prepared data is then seamlessly passed to the UnpackMol WaNo within the ForEach loop control, further enhancing the efficiency of your workflow process.

UnpackMol. The UnpackMol WaNo is designed to efficiently uncompress configuration files generated by SOD-2022, preparing them for subsequent processing with the DFT-VASP WaNo. UnpackMol is seamlessly integrated with the SimStack framework within the ForEach loop control. This combination enhances the efficiency of handling and preparing multiple configurations, ensuring a smooth and automated transition from the SOD-2022 output to the DFT-VASP WaNo input. This integration is vital to our workflow, streamlining the data preparation process for density functional theory calculations.

DFT-VASP. This WaNo is specifically developed to facilitate Density Functional Theory (DFT) calculations through the Vienna Ab initio Simulation Package (VASP) code[68,69]. This WaNo is tailored for researchers who may or may not be familiar with the intricate functionalities of VASP, simplifying the optimization process of these calculations.

Our total energy calculations and structural optimizations are grounded in DFT, as formulated by Hohenberg and Kohn and Kohn and Sham[70,71]. We utilize the semilocal Perdew–Burke–Ernzerhof (PBE) approximation for the exchange-correlation energy functional, as proposed by Perdew et al.[72] and implemented in VASP[68,69]. The Kohn-Sham equations are solved using the Projector Augmented-Wave (PAW) method (Blöchl)[73], with core states addressed through fully relativistic calculations and valence states via a scalar-relativistic approximation, inclusive of Spin-Orbit Coupling (SOC).

For all systems, the PAW framework expands plane waves to a cutoff energy of 500 eV. The valence electron configurations are as follows: Cs ($5s^2, 5p^6, 6s^1$), H ($1s^1$), C ($2s^2, 2p^2$), N ($2s^2, 2p^3$), Pb ($5s^2, 5d^{10}, 6s^2, 6p^2$), and I ($5s^2, 5p^5$). For the $2 \times 2 \times 2$ supercell expansion from a unit cell, the Brillouin zone integration is executed with a $4 \times 4 \times 4$ k-mesh. We set the total energy convergence criterion at e-5 eV. Additionally, the lattice constants and stress tensors are fully optimized, ensuring that the Hellmann-Feynman forces on each atom are relaxed to values below 0.010 eV $Å^{-1}$.

DB-Generator. This WaNo is designed to produce files in yml format, comprehensively detailing the degeneracy factors and total energies derived from DFT-VASP calculations. These files are crucial for the subsequent stages of our workflow. They will be automatically loaded into a Colab notebook, which serves as the data set for calculating alloys' phase diagrams and assessing their respective properties. This integration ensures a seamless transition from energy calculations to analyzing these phase diagrams, facilitating a more efficient and accurate determination of alloy properties.

Thermodynamic, electronic and structural properties through a colab notebook

Within GQCA approach[17,36,65], the probability x_j of each configuration j as part of the ensemble can be estimated by the minimization of the Helmholtz free energy, $\Delta F_{\mathrm{mix}}(x, T)$, for the mixing of the $A_{1-x}Cs_xPbI_3$ perovskite alloys (A = MA, FA), so that

$$\Delta F_{\mathrm{mix}} = \Delta U_{\mathrm{mix}}(x, T) - T\Delta S_{\mathrm{mix}}(x, T) \tag{1}$$

so that $\Delta U_{\mathrm{mix}}(x, T)$ is the mixing internal energy defined by

$$\Delta U_{\mathrm{mix}}(x, T) = \sum_{j=1}^{J} x_j(x, T)\Delta\varepsilon_j \tag{2}$$

where $\Delta\varepsilon_j$ is the excess energy of j-th class, calculated as

$$\Delta\varepsilon_j = E_j - \frac{n - n_j}{n}E_{\mathrm{APbI_3}} - \frac{n_j}{n}E_{\mathrm{CsPbI_3}}. \tag{3}$$

Here, $E_j, E_{\mathrm{APbI_3}}$, and $E_{\mathrm{CsPbI_3}}$ are the total energies of j-th configuration (class), $APbI_3$ (A = MA or FA) and $CsPbI_3$, respectively, considering as a reference for the pristine compounds their stablest configuration in the corresponding ensemble. n and n_j stand for the total number of cuboctahedral sites in the supercell (8 sites) corresponding to the number of Cs cations (see Supplementary Table 1). In Eq. (2), x_j accounts the cluster probability defined by[74]

$$x_j(x, T) = \frac{g_j\eta^{n_j}\mathrm{e}^{-\beta\Delta\varepsilon_j}}{\sum_{i=1}^{J} g_i\eta^{n_i}\mathrm{e}^{-\beta\Delta\varepsilon_i}} \tag{4}$$

in which $\beta = (k_B T)^{-1}$ where T is temperature (and k_B is the Boltzmann constant), g_j is the degeneracy factor of j-th class obtained at WaNo SOD-2022 and η is a parameter defined by the constrain $\sum_j x_j(x, T)n_j = nx$. In the case of APD, we also defined the polymorph probability as $x_k = \sum_{j\in k} x_j$, with $k = a^-a^-a^+, a^-a^-a^-$ or ROT and the sum is over all cluster associated with

the corresponding polymorph pattern. Following this, we employed a mixing entropy based on the Kullback–Leibler (KL)[75] divergence as

$$D_{\mathrm{KL}}(x_j||x_j^0) = \sum_{j=1}^{J} x_j \ln\left(\frac{x_j}{x_j^0}\right) \tag{5}$$

where $x_j^0 = g_j x^{n_j}(1-x)^{n-n_j}$ is the probability distribution for the j-th class in a regular solid solution with the proper normalization to account for the number of polymorphs[36], leading to the mixing entropy expression as

$$\begin{aligned}\Delta S_{\mathrm{mix}} &= -Nk_{\mathrm{B}}[x\ln x + (1-x)\ln(1-x)] \\ &\quad -Mk_{\mathrm{B}}D_{\mathrm{KL}}\left(x_j||x_j^0\right)\end{aligned} \tag{6}$$

in which N is the total number of cuboctahedral sites in the solid solution, and M is the total number of clusters in the alloy. According to previous works, this expression is suggested to be sufficient for calculating the thermodynamic properties of MHP alloys in good accordance with experiments[16,17,76,77], while for other systems, vibrational and magnetic contributions could affect their stability and, if this happens, they should also be included in the entropy expression[78,79].

Based on the expression of ΔF_{mix}, T-x phase diagrams can be constructed by calculating spinodal and binodal lines, as described in Section III of the Supporting Information. Following the Connolly-Williams method[65,80], electronic and structural properties (P) of alloys can be calculated as an average over the statistical ensemble from the MHP alloy configurations, i.e.,

$$P(x,T) = \sum_{j=1}^{J} x_j(x,T)P_j \tag{7}$$

where $P(x, T)$ stands for lattice parameters (a, b and c), Pb-I distances, Pb-I-Pb angles, gap energies (E_g), among others. All the equations above were implemented in a Colab Notebook, which can be accessed on our GitHub platform (https://github.com/Alloys-Workflow).

Gap energy from DFT-1/2 quasiparticle correction

Gap energies (E_g) were calculated through a quasiparticle correction based on Slater's half-ion technique[81,82], named DFT-1/2[83]. Our previous works have demonstrated the efficiency of the DFT-1/2 transferability adopted here[17,19,64], in which the half-ionization in the representative configurations of the alloys (associated with the 5p state from the I) was performed, modifying the standard Kohn-Sham (KS) potential ($V_{\mathrm{KS}}(\mathbf{r})$) by subtracting from it the electronic self-energy potential ($V_S(\mathbf{r})$), i.e., $V_{\mathrm{mod,KS}}(\mathbf{r}) = V_{\mathrm{KS}}(\mathbf{r}) - V_S(\mathbf{r})$.

$V_S(\mathbf{r})$ was approximated via $V_S(\mathbf{r}) = \Theta(\mathbf{r}, \mathrm{CUT})[V_0(\mathbf{r}) - V_{-1/2}(\mathbf{r})]$, with $V_0(\mathbf{r})$ and $V_{-1/2}(\mathbf{r})$ denoting the KS potential for the neutral and half-ionized iodine atoms, respectively. The step function $\Theta(\mathbf{r}, \mathrm{CUT})$ was introduced to avoid interpenetration between neighbor atoms, whose CUT parameter is determined variationally by maximizing the gap energy without empirical parameters[17,64]. CUT parameters were independently optimized to $CsPbI_3$, $MAPbI_3$, and $FAPbI_3$, but coincidentally it reaches $3.85a_0$, as depicted in Supplementary Fig. 2 of the Supporting Information, so that the same value was adopted to all $MA_{1-x}Cs_xPbI_3$ and $FA_{1-x}Cs_xPbI_3$ here studied. Finally, the approximated quasiparticle correction described here, when combined with SOC (DFT-1/2+SOC protocol), leads to results in similar accuracy to those obtained via the expensive GW approach but with standard DFT costs. More details about the DFT-1/2 approach can be accessed in Section IV of the Supporting Information.

PCE calculations via Spectroscopic Limited Maximum Efficiency (SLME) model

We employed the Spectroscopic Limited Maximum Efficiency (SLME) model[84] to calculate the maximum PCE of our alloys' polymorphs via GQCA statistics, considering a MHP alloy width of 1 μm at 300 K. SLME is based on the principle of detailed balance, differing from the Shockley–Queisser (SQ) model by explicitly considering the specific absorption coefficient of the material, as reported by previous studies[85–87]. Details about the model are available in Section V of the Supporting Information. Here, we computed the PCE through the SLME model for all $J = 22$ cluster classes, expanding each polymorph representing the $A_{1-x}Cs_xPbI_3$ alloys by using[88,89]

$$\alpha_j(\omega) = \frac{\sqrt{2}\omega}{c}\left[\sqrt{\epsilon_{\mathrm{Re},j}^2(\omega) + \epsilon_{\mathrm{Im},j}^2(\omega)} - \epsilon_{\mathrm{Re},j}(\omega)\right]^{1/2} \tag{8}$$

as absorption coefficient – $\alpha_j(\omega)$ – through Random Phase Approximation (RPA)[90] from the DFT-1/2 + SOC protocol employed to calculate E_g. The expression for $\alpha_j(\omega)$ is defined by $\hbar\omega$ as the photon energy, c the speed of light in vacuum, $\epsilon_{\mathrm{Re},j}(\omega)$ the real part, and $\epsilon_{\mathrm{Im},j}(\omega)$ the imaginary part of the dielectric function. $\epsilon_{\mathrm{Im},j}(\omega)$ was calculated employing the RPA, while $\epsilon_{\mathrm{Re},j}(\omega)$ was obtained via Kramers–Kronig transformation[91]. After that, the absorption coefficients for alloys' polymorphs were obtained as GQCA averages over their respective ensembles, i.e. $\alpha(\omega; x, T) = \sum_{\forall j} x_j(x,T)\alpha_j(\omega)$[17].

Data availability

The data that supports the findings of this study are available at https://github.com/Alloys-Workflowor from the corresponding author upon reasonable request.

Code availability

The code supporting this study's findings is available at https://github.com/Alloys-Workflow.

Received: 22 December 2023; Accepted: 14 June 2024;
Published online: 04 July 2024

References

1. Park, J. et al. Controlled Growth of Perovskite Layers with Volatile Alkylammonium Chlorides. *Nature* **616**, 724–730 (2023).
2. Koh, T. M. et al. Formamidinium-Containing Metal-Halide: An Alternative Material for Near-IR Absorption Perovskite Solar Cells. *J. Phys. Chem. C* **118**, 16458–16462 (2014).
3. Yang, J. & Kelly, T. L. Decomposition and Cell Failure Mechanisms in Lead Halide Perovskite Solar Cells. *Inorg. Chem.* **56**, 92–101 (2017).
4. Niu, T., Chao, L., Dong, X., Fu, L. & Chen, Y. Phase-Pure α-$FAPbI_3$ for Perovskite Solar Cells. *J. Phys. Chem. Lett.* **13**, 1845–1854 (2022).
5. Choi, H. et al. Cesium-Doped Methylammonium Lead Iodide Perovskite Light Absorber for Hybrid Solar Cells. *Nano Energy* **7**, 80–85 (2014).
6. Lee, J.-W. et al. Formamidinium and Cesium Hybridization for Photo- and Moisture-Stable Perovskite Solar Cell. *Adv. Energy Mater.* **5**, 1501310 (2015).
7. Li, Z. et al. Stabilizing Perovskite Structures by Tuning Tolerance Factor: Formation of Formamidinium and Cesium Lead Iodide Solid-State Alloys. *Chem. Mater.* **28**, 284–292 (2016).
8. Niu, G., Li, W., Li, J., Liang, X. & Wang, L. Enhancement of Thermal Stability for Perovskite Solar Cells through Cesium Doping. *RSC Adv.* **7**, 17473–17479 (2017).
9. Du, S. et al. Incorporation of Cesium Ions into $MA_{1-x}Cs_xPbI_3$ Single Crystals: Crystal Growth, Enhancement of Stability, and Optoelectronic Properties. *J. Phys. Chem. Lett.* **9**, 5833–5839 (2018).
10. Charles, B. et al. Phase Behavior and Substitution Limit of Mixed Cesium-Formamidinium Lead Triiodide Perovskites. *Chem. Mater.* **32**, 2282–2291 (2020).
11. Dalpian, G. M., Zhao, X., Kazmerski, L. & Zunger, A. Formation and Composition-Dependent Properties of Alloys of Cubic Halide Perovskites. *Chem. Mater.* **31**, 2497–2506 (2019).

12. Zhao, X., Dalpian, G. M., Wang, Z. & Zunger, A. Polymorphous Nature of Cubic Halide Perovskites. *Phys. Rev. B* **101**, 155137 (2020).
13. Zhao, X.-G., Wang, Z., Malyi, O. I. & Zunger, A. Effect of Static Local Distortions vs. Dynamic Motions on the Stability and Band Gaps of Cubic Oxide and Halide Perovskites. *Mater. Today* **49**, 107–122 (2021).
14. de Araujo, L. O. et al. How Cation Nature Controls the Bandgap and Bulk Rashba Splitting of Halide Perovskites. *J. Comput. Chem.* **44**, 1395–1403 (2023).
15. Schleife, A. et al. Ab initio description of heterostructural alloys: Thermodynamic and structural properties of $Mg_xZn_{1-x}O$ and $Cd_xZn_{1-x}O$. *Phys. Rev. B* **81**, 245210 (2010).
16. Guedes-Sobrinho, D., Guilhon, I., Marques, M. & Teles, L. K. Thermodynamic Stability and Structural Insights for $CH_3NH_3Pb_{1-x}Si_xI_3$, $CH_3NH_3Pb_{1-x}Ge_xI_3$, and $CH_3NH_3Pb_{1-x}Sn_xI_3$ Hybrid Perovskite Alloys: A Statistical Approach from First Principles Calculations. *Sci. Rep.* **9**, 11061 (2019).
17. Guedes-Sobrinho, D., Guilhon, I., Marques, M. & K. Teles, L. Relativistic DFT-1/2 Calculations Combined with a Statistical Approach for Electronic and Optical Properties of Mixed Metal Hybrid Perovskites. *J. Phys. Chem. Lett.* **10**, 4245–4251 (2019).
18. Yang, R. X., Skelton, J. M., da Silva, E. L., Frost, J. M. & Walsh, A. Spontaneous Octahedral Tilting in the Cubic Inorganic Cesium Halide Perovskites $CsSnX_3$ and $CsPbX_3$ (X = F, Cl, Br, I). *J. Phys. Chem. Lett.* **8**, 4720–4726 (2017).
19. de Araujo, L. O., Rêgo, C. R. C., Wenzel, W., Sabino, F. P. & Guedes-Sobrinho, D. Impact of the Polymorphism and Relativistic Effects on the Electronic Properties of Inorganic Metal Halide Perovskites. *J. Phys. Chem. C* **126**, 2131–2140 (2022).
20. Dias, A. C., Lima, M. P. & Da Silva, J. L. F. Role of Structural Phases and Octahedra Distortions in the Optoelectronic and Excitonic Properties of $CsGeX_3$ (X = Cl, Br, I) Perovskites. *J. Phys. Chem. C* **125**, 19142–19155 (2021).
21. Hao, F., Stoumpos, C. C., Chang, R. P. H. & Kanatzidis, M. G. Anomalous Band Gap Behavior in Mixed Sn and Pb Perovskites Enables Broadening of Absorption Spectrum in Solar Cells. *J. Am. Chem. Soc.* **136**, 8094–8099 (2014).
22. Ogomi, Y. et al. $CH_3NH_3Sn_xPb_{1-x}I_3$ Perovskite Solar Cells Covering up to 1060 nm. *J. Phys. Chem. Lett.* **5**, 1004–1011 (2014).
23. Khatun, S., Maiti, A. & Pal, A. J. Bowing of Transport Gap in Hybrid Halide Perovskite Alloys ($CH_3NH_3Sn_{1-x}Pb_xI_3$): Which Band is Responsible? *Appl. Phys. Lett.* **116**, 012104 (2020).
24. Muscarella, L. A. et al. Lattice Compression Increases the Activation Barrier for Phase Segregation in Mixed-Halide Perovskites. *ACS Energy Lett.* **5**, 3152–3158 (2020).
25. Lu, L. et al. Interaction of the Cation and Vacancy in Hybrid Perovskites Induced by Light Illumination. *ACS Appl. Mater. Interfaces* **12**, 42369–42377 (2020).
26. Prasanna, R. et al. Band Gap Tuning via Lattice Contraction and Octahedral Tilting in Perovskite Materials for Photovoltaics. *J. Am. Chem. Soc.* **139**, 11117–11124 (2017).
27. Imran, M., Saleem, A., Khan, N. A. & Kamboh, A. H. Enhanced Efficiency and Stability of Perovskite Solar Cells by Partial Replacement of $CH_3NH_3^+$ with Inorganic Cs^+ in $CH_3NH_3PbI_3$ Perovskite Absorber Layer. *Physica B Condens. Matter* **572**, 1–11 (2019).
28. Saidaminov, M. I. et al. High-Quality Bulk Hybrid Perovskite Single Crystals within Minutes by Inverse Temperature Crystallization. *Nat. Commun*. **6**, 7586 (2015).
29. Ferdani, D. W. et al. Partial Cation Substitution Reduces Iodide Ion Transport in Lead Iodide Perovskite Solar Cells. *Energy Environ. Sci.* **12**, 2264–2272 (2019).
30. Wei, Q. et al. Metal Halide Perovskite Alloy: Fundamental, Optoelectronic Properties and Applications. *Adv. Photonics Res.* **4**, 2200236 (2022).
31. Grau-Crespo, R., Hamad, S., Catlow, C. R. A. & Leeuw, N. H. D. Symmetry-Adapted Configurational Modelling of Fractional Site Occupancy in Solids. *J. Phys. Condens. Matter* **19**, 256201 (2007).
32. Umari, P., Mosconi, E. & De Angelis, F. Relativistic GW Calculations on $CH_3NH_3PbI_3$ and $CH_3NH_3SnI_3$ Perovskites for Solar Cell Applications. *Sci. Rep.* **4**, 4467 (2014).
33. Mosconi, E., Umari, P. & Angelis, F. D. Electronic and Optical Properties of Mixed Sn–Pb Organohalide Perovskites: a First Principles Investigation. *J. Mater. Chem. A* **3**, 9208–9215 (2015).
34. Leppert, L., Rangel, T. & Neaton, J. B. Towards Predictive Band Gaps for Halide Perovskites: Lessons from One-Shot and Eigenvalue Self-Consistent GW. *Phys. Rev. Mater.* **3**, 103803 (2019).
35. Wierzbowska, M. & Meléndez, J. J. Role of Inorganic Cations in the Excitonic Properties of Lead Halide Perovskites. *Phys. Chem. Chem. Phys.* **25**, 2468–2476 (2023).
36. Sher, A., van Schilfgaarde, M., Chen, A. & Chen, W. Quasichemical Approximation in Binary Alloys. *Phys. Rev. B* **36**, 4279–4295 (1987).
37. Hu, H., Dong, B. & Zhang, W. Low-toxic metal halide perovskites: opportunities and future challenges. *J. Mater. Chem. A* **5**, 11436–11449 (2017).
38. Rêgo, C. R. C. et al. SimStack: An Intuitive Workflow Framework. *Front. Mater.* **9**, 877597 (2022).
39. Schaarschmidt, J. et al. Workflow Engineering in Materials Design within the BATTERY 2030 + Project. *Adv. Energy Mater.* **12**, 2102638 (2021).
40. Mostaghimi, M. et al. Automated Virtual Design of Organic Semiconductors Based on Metal-Organic Frameworks. *Front. Mater.* **9**, 840644 (2022).
41. Yi, C. et al. Entropic Stabilization of Mixed A-Cation abx_3 Metal Halide Perovskites for High Performance Perovskite Solar Cells. *Energy Environ. Sci.* **9**, 656–662 (2016).
42. Dong, D. et al. Bandgap Tunable $Cs_x(CH_3NH_3)_{1-x}PbI_3$ Perovskite Nanowires by Aqueous Solution Synthesis for Optoelectronic Devices. *Nanoscale* **9**, 1567–1574 (2017).
43. Zhang, Y., Grancini, G., Feng, Y., Asiri, A. M. & Nazeeruddin, M. K. Optimization of Stable Quasi-Cubic $FA_xMA_{1-x}PbI_3$ Perovskite Structure for Solar Cells with Efficiency beyond 20%. *ACS Energy Lett.* **2**, 802–806 (2017).
44. Weller, M. T., Weber, O. J., Henry, P. F., Di Pumpo, A. M. & Hansen, T. C. Complete Structure and Cation Orientation in the Perovskite Photovoltaic Methylammonium Lead Iodide Between 100 and 352 K. *Chem. Commun.* **51**, 4180–4183 (2015).
45. Weller, M. T., Weber, O. J., Frost, J. M. & Walsh, A. Cubic Perovskite Structure of Black Formamidinium Lead Iodide, α-$HC(NH_2)_2PbI_3$, at 298 K. *J. Phys. Chem. Lett.* **6**, 3209–3212 (2015).
46. Sharma, S., Weiden, N. & Weiss, A. Phase Diagrams of Quasibinary Systems of the Type: ABX_3–$A'BX_3$; ABX_3–$AB'X_3$, and ABX_3–ABX'_3. *Z. Phys. Chem.* **175**, 63–80 (1992).
47. Denton, A. R. & Ashcroft, N. W. Vegard's Law. *Phys. Rev. A* **43**, 3161–3164 (1991).
48. Friedel, J. LX. Deviations from Vegard's Law. *Lond. Edinb. Dublin Philos. Mag. J. Sci.* **46**, 514–516 (1955).
49. Kieslich, G., Sun, S. & Cheetham, A. K. Solid-State Principles Applied to Organic-Inorganic Perovskites: New Tricks for an Old Dog. *Chem. Sci.* **5**, 4712–4715 (2014).
50. Kim, J. Y., Lee, J.-W., Jung, H. S., Shin, H. & Park, N.-G. High-Efficiency Perovskite Solar Cells. *Chem. Rev.* **120**, 7867–7918 (2020).
51. Amat, A. et al. Cation-Induced Band-Gap Tuning in Organohalide Perovskites: Interplay of Spin-Orbit Coupling and Octahedra Tilting. *Nano Lett.* **14**, 3608–3616 (2014).
52. Chen, Q. et al. Under the Spotlight: The Organic–Inorganic Hybrid Halide Perovskite for Optoelectronic Applications. *Nano Today* **10**, 355–396 (2015).

53. Franssen, W. M. J., van Es, S. G. D., Dervişoğlu, R., de Wijs, G. A. & Kentgens, A. P. M. Symmetry, Dynamics, and Defects in Methylammonium Lead Halide Perovskites. *J. Phys. Chem. Lett.* **8**, 61–66 (2017).
54. Wang, Y. et al. Cation Dynamics Governed Thermal Properties of Lead Halide Perovskite Nanowires. *Nano Lett.* **18**, 2772–2779 (2018).
55. Leguy, A. M. A. et al. The Dynamics of Methylammonium Ions in Hybrid Organic-Inorganic Perovskite Solar Cells. *Nat. Commun.* **6**, 7124 (2015).
56. Bonadio, A. et al. Entropy-Driven Stabilization of the Cubic Phase of $MAPbI_3$ at Room Temperature. *J. Mater. Chem. A* **9**, 1089–1099 (2021).
57. Huang, J., Xu, P., Liu, J. & You, X.-Z. Sequential Introduction of Cations Deriving Large-Grain $Cs_xFA_{1-x}PbI_3$ Thin Film for Planar Hybrid Solar Cells: Insight into Phase-Segregation and Thermal-Healing Behavior. *Small* **13**, 1603225 (2016).
58. Kubicki, D. J. et al. Phase Segregation in Cs^-, Rb^- and K^- Doped Mixed-Cation $(MA)_x(FA)_{1-x}PbI_3$ Hybrid Perovskites from Solid-State NMR. *J. Am. Chem. Soc.* **139**, 14173–14180 (2017).
59. Liu, L. et al. A-site Phase Segregation in Mixed Cation Perovskite. *Mater. Rep. Energy* **1**, 100064 (2021).
60. Bartel, C. J. Review of Computational Approaches to Predict the Thermodynamic Stability of Inorganic Solids. *J. Mater. Sci.* **57**, 10475–10498 (2022).
61. Kittel, C., Kroemer, H. *Thermal Physics*, 2nd edn. (W. H. Freeman, 1980).
62. Maheshwari, S., Patwardhan, S., Schatz, G. C., Renaud, N. & Grozema, F. C. The Effect of the Magnitude and Direction of the Dipoles of Organic Cations on the Electronic Structure of Hybrid Halide Perovskites. *Phys. Chem. Chem. Phys.* **21**, 16564–16572 (2019).
63. Xu, Z. et al. Phase Diagram and Stability of Mixed-Cation Lead Iodide Perovskites: A Theory and Experiment Combined Study. *Phys. Rev. Mater.* **4**, 095401 (2020).
64. de Araujo, L. O., Sabino, F. P., Rêgo, C. R. C. & Guedes-Sobrinho, D. Bulk Rashba Effect Splitting and Suppression in Polymorphs of Metal Iodine Perovskites. *J. Phys. Chem. Lett.* **12**, 7245–7251 (2021).
65. Teles, L. K., Furthmüller, J., Scolfaro, L. M. R., Leite, J. R. & Bechstedt, F. First-principles Calculations of the Thermodynamic and Structural Properties of Strained $In_xGa_{1-x}N$ and $Al_xGa_{1-x}N$ Alloys. *Phys. Rev. B* **62**, 2475–2485 (2000).
66. Guilhon, I., Teles, L. K., Marques, M., Pela, R. R. & Bechstedt, F. Influence of Structure and Thermodynamic Stability on Electronic Properties of Two-Dimensional SiC, SiGe, and GeC Alloys. *Phys. Rev. B* **92**, 075435 (2015).
67. Glazer, A. M. The Classification of Tilted Octahedra in Perovskites. *Acta Crystallogr. Sect. B Struct. Crystallogr. Cryst. Chem.* **28**, 3384–3392 (1972).
68. Kresse, G. & Hafner, J. Ab Initio Molecular Dynamics for Open–Shell Transition Metals. *Phys. Rev. B* **48**, 13115–13118 (1993).
69. Kresse, G. & Furthmüller, J. Efficient Iterative Schemes for Ab Initio Total-Energy Calculations Using a Plane-Wave Basis Set. *Phys. Rev. B* **54**, 11169–11186 (1996).
70. Hohenberg, P. & Kohn, W. Inhomogeneous Electron Gas. *Phys. Rev.* **136**, B864–B871 (1964).
71. Kohn, W. & Sham, L. J. Self-Consistent Equations Including Exchange and Correlation Effects. *Phys. Rev.* **140**, A1133–A1138 (1965).
72. Perdew, J. P., Burke, K. & Ernzerhof, M. Generalized Gradient Approximation Made Simple. *Phys. Rev. Lett.* **77**, 3865–3868 (1996).
73. Blöchl, P. E. Projector Augmented-Wave Method. *Phys. Rev. B* **50**, 17953–17979 (1994).
74. Borlido, P., Bechstedt, F., Botti, S. & Rödl, C. Ensemble Averages of Ab Initio Optical, Transport, and Thermoelectric Properties of Hexagonal Si_xGe_{1-x} Alloys. *Phys. Rev. Mater.* **7**, 014602 (2023).
75. Kullback, S. & Leibler, R. A. On Information and Sufficiency. *Ann. Math. Statist.* **22**, 79–86 (1951).
76. Brivio, F., Caetano, C. & Walsh, A. Thermodynamic origin of photoinstability in the $CH_3NH_3Pb(I_{1-x}Br_x)_3$ hybrid halide perovskite alloy. *J. Phys. Chem. Lett.* **7**, 1083–1087 (2016).
77. Valadares, F., Guilhon, I., Teles, L. K. & Marques, M. Atomistic Origins of Enhanced Band Gap, Miscibility, and Oxidation Resistance in α-$CsPb_{1-x}Sn_xI_3$ Mixed Perovskite. *J. Phys. Chem.* **124**, 26124–26133 (2020).
78. Tian, F. A Review of Solid-Solution Models of High-Entropy Alloys Based on Ab Initio Calculations. *Front. Mater.* **4**, 36 (2017).
79. Esters, M. et al. Settling the Matter of the Role of Vibrations in the Stability of High-Entropy Carbides. *Nat. Commun.* **12**, 5747 (2021).
80. Connolly, J. W. D. & Williams, A. R. Density-Functional Theory Applied to Phase Transformations in Transition-Metal Alloys. *Phys. Rev. B* **27**, 5169–5172 (1983).
81. Slater, J. C. & Johnson, K. H. Self-Consistent-Field X–α Cluster Method for Polyatomic Molecules and Solids. *Phys. Rev. B* **5**, 844–853 (1972).
82. Ferreira, L. G., Marques, M. & Teles, L. K. Slater Half-Occupation Technique Revisited: The LDA-1/2 and GGA-1/2 Approaches for Atomic Ionization Energies and Band Gaps in Semiconductors. *AIP Adv.* **1**, 032119 (2011).
83. Ferreira, L. G., Marques, M. & Teles, L. K. Approximation to Density Functional Theory for the Calculation of Band Gaps of Semiconductors. *Phys. Rev. B* **78**, 125116 (2008).
84. Yu, L. & Zunger, A. Identification of Potential Photovoltaic Absorbers Based on First-Principles Spectroscopic Screening of Materials. *Phys. Rev. Lett.* **108**, 068701 (2012).
85. Silveira, J. F. R. V., Besse, R., Dias, A. C., Caturello, N. A. M. S. & Da Silva, J. L. F. Tailoring Excitonic and Optoelectronic Properties of Transition Metal Dichalcogenide Bilayers. *J. Phys. Chem. C* **126**, 9173–9184 (2022).
86. Moujaes, E. A. & Dias, A. C. On the excitonic effects of the 1T and 1OT phases of PdS_2, $PdSe_2$, and PdSSe monolayers. *J. Phys. Chem. Solids* **182**, 111573 (2023).
87. dos Santos, R. M., Ornelas-Cruz, I., Dias, A. C., Lima, M. P. & Da Silva, J. L. F. Theoretical Investigation of the Role of Mixed A^+ Cations in the Structure, Stability, and Electronic Properties of Perovskite Alloys. *ACS Appl. Energy Mater.* **6**, 5259–5273 (2023).
88. Barhoumi, M. First-Principles Calculations to Investigate Electronic Band Structure, Optical and Mechanical Properties of New CaFCl Monolayer. *Results. Phys.* **45**, 106251 (2023).
89. Diery, W. Electronic and Optical Properties of New Pentagonal Janus PtXY (X, Y=S, Se, Te; $X \neq Y$) Monolayers: A DFT Study. *Physica B Condens. Matter* **669**, 415308 (2023).
90. Gajdoš, M., Hummer, K., Kresse, G., Furthmüller, J. & Bechstedt, F. Linear Optical Properties in the Projector-Augmented Wave Methodology. *Phys. Rev. B* **73**, 045112 (2006).
91. Hu, B. Y. Kramers-Kronig in Two Lines. *Am. J. Phys.* **57**, 821–821 (1989).
92. Quarti, C. et al. Structural and Optical Properties of Methylammonium Lead Iodide Across the Tetragonal to Cubic Phase Transition: Implications for Perovskite Solar Cells. *Energy Environ. Sci.* **9**, 155–163 (2016).
93. Palazon, F. et al. Room-Temperature Cubic Phase Crystallization and High Stability of Vacuum- Deposited Methylammonium Lead Triiodide Thin Films for High-Efficiency Solar Cells. *Adv. Mater.* **31**, 1902692 (2019).

Acknowledgements

The authors thank the Atos and Yemoja Computer at CIMATEC SENAI (Salvador – BA) and "Laboratório Central de Processamento de Alto Desempenho" (LCPAD) financed by FINEP through CT-INFRA/UFPR projects in Brazil to support the electronic structure calculations. Part of this work was performed on the HoreKa supercomputer funded by the Ministry

of Science, Research and the Arts Baden-Württemberg and by the Federal Ministry of Education and Research. L.O.A. thanks the Coordination for Improvement of Higher Level Education – CAPES (finance Code 001) for funding. M.J.P. thanks the National Council for Scientific and Technological Development – CNPq (grant number 307345/2021-1). W.W. and C.R.C.R. thank the German Federal Ministry of Education and Research (BMBF) for financial support of the project Innovation-Platform MaterialDigital (www.materialdigital.de) through project funding FKZ number 13XP5094A. A.C.D. thanks the financial support from the National Council for Scientific and Technological Development (CNPq, 408144/2022-0), Federal District Research Support Foundation (FAPDF, grant 00193-00001817/2023-43), and also the computational resources from "Centro Nacional de Processamento de Alto Desempenho em São Paulo" (CENAPAD-SP, UNICAMP/FINEP - MCTI project) for resources into 897 project, Lobo Carneiro HPC (NACAD) at the Federal University of Rio de Janeiro (UFRJ) into 133 project. We acknowledge support by the KITPublication Fund of the Karlsruhe Institute of Technology.

Author contributions

L.O.A. carried out the DFT calculations, wrote the code for GQCA calculations in the Colab notebook, analyzed the data, made the graphs, and wrote the first version of the manuscript. C.R.C.R. contributed to coding the GQCA in the Colab notebook and the WaNos for automation tools via the SimStack framework. W.W. helped develop ideas and computational resources. M.J.P. helped develop ideas, analyze data, and revise the manuscript. A.C.D. helped develop ideas, wrote the code for PCE calculations via SLME, and helped with data analysis. D.G.S. supervised the work, helped develop ideas and their analysis, and wrote the manuscript. All authors contribute to writing and revising the manuscript.

Funding

Open Access funding enabled and organized by Projekt DEAL.

Competing interests

The authors declare no competing interests.

Additional information

Supplementary information The online version contains supplementary material available at https://doi.org/10.1038/s41524-024-01320-8.

Correspondence and requests for materials should be addressed to Luis Octavio de Araujo, Celso R. C. Rêgo, Wolfgang Wenzel, Maurício Jeomar Piotrowski, Alexandre Cavalheiro Dias or Diego Guedes-Sobrinho.